Chemical Science

EDGE ARTICLE

Alloying a single and a double perovskite: a Cu$^{+/2+}$ mixed-valence layered halide perovskite with strong optical absorption†

Bridget A. Connor,[a] Rebecca W. Smaha, [ID][ab] Jiayi Li,[a] Aryeh Gold-Parker, [ID][ac] Alexander J. Heyer, [ID][a] Michael F. Toney, [ID][cd] Young S. Lee [ID][be] and Hemamala I. Karunadasa [ID]*[ab]

Introducing heterovalent cations at the octahedral sites of halide perovskites can substantially change their optoelectronic properties. Yet, in most cases, only small amounts of such metals can be incorporated as impurities into the three-dimensional lattice. Here, we exploit the greater structural flexibility of the two-dimensional (2D) perovskite framework to place three distinct stoichiometric cations in the octahedral sites. The new layered perovskites $A^I_4[Cu^{II}(Cu^IIn^{III})_{0.5}Cl_8]$ (**1**, A = organic cation) may be derived from a Cu^I–In^{III} double perovskite by replacing half of the octahedral metal sites with Cu^{2+}. Electron paramagnetic resonance and X-ray absorption spectroscopy confirm the presence of Cu^{2+} in **1**. Crystallographic studies demonstrate that **1** represents an averaging of the Cu^I–In^{III} double perovskite and Cu^{II} single perovskite structures. However, whereas the highly insulating Cu^I–In^{III} and Cu^{II} perovskites are colorless and yellow, respectively, **1** is black, with substantially higher electronic conductivity than that of either endmember. We trace these emergent properties in **1** to intervalence charge transfer between the mixed-valence Cu centers. We further propose a tiling model to describe how the Cu$^+$, Cu^{2+}, and In^{3+} coordination spheres can pack most favorably into a 2D perovskite lattice, which explains the unusual 1 : 2 : 1 ratio of these cations found in **1**. Magnetic susceptibility data of **1** further corroborate this packing model. The emergence of enhanced visible light absorption and electronic conductivity in **1** demonstrates the importance of devising strategies for increasing the compositional complexity of halide perovskites.

1. Introduction

The double perovskite lattice considerably increases the versatility of halide perovskites by enabling the incorporation of a much wider range of elements compared to single perovskites. Here, the divalent octahedral B-site cation of the three-dimensional (3D) $A^IB^{II}X_3$ (X = halide) single perovskite structure is replaced with an ordered mixture of two different B-site occupants, yielding the general formula $A^I_2BB'X_6$. Nevertheless, the double perovskite framework is still restrictive in that it requires exactly two distinct B-sites that satisfy charge balance requirements.[1] Thus, double perovskites most commonly feature B-site combinations of 1+ and 3+ (*e.g.*, $Cs_2Ag^IBi^{III}Br_6$)[2,3] or 4+ and 0 (vacancy) (*e.g.*, $Cs_2Sn^{IV}Cl_6$).[4] Recent work has explored B-site alloying as a means of further expanding the compositional phase space of double perovskites.[5–7] Isovalent alloying, in which the impurity cation carries the same charge as one of the two B-site cations, is a highly effective method for tuning the optical and electronic properties of these materials. Often, such alloys exist as solid solutions where the composition and materials properties can be varied continuously between two pure endmember phases.[5,8–11] Aliovalent alloying, in which the charge of the impurity cation does not match the charge of either B-site cation, can have a similarly large impact on the properties of a given double perovskite composition.[7,12–14] However, compositional flexibility approaching that seen in isovalent alloys remains rare.[15,16] Likely due to lattice mismatch, local charge imbalances, and formation of charge-compensating defects,[7] most examples of aliovalent alloys exist only in a narrow composition window with low (*ca.* 1

[a]Department of Chemistry, Stanford University, Stanford, California 94305, USA. E-mail: hemamala@stanford.edu

[b]Stanford Institute for Materials and Energy Sciences, SLAC National Accelerator Laboratory, Menlo Park, California 94025, USA

[c]Stanford Synchrotron Radiation Lightsource, SLAC National Accelerator Laboratory, Menlo Park, California 94025, USA

[d]Department of Chemical and Biological Engineering, University of Colorado Boulder, Boulder, CO 80309, USA

[e]Department of Applied Physics, Stanford University, Stanford, California 94305, USA

atom%) impurity concentrations. Nevertheless, complex perovskite compositions, which incorporate heterovalent cations in high concentrations, may exhibit unique optoelectronic properties and strategies for their syntheses are, therefore, highly desirable.

The close structural analogy between halide perovskites and their oxide analogues points to one exciting avenue for such work. Layered Cu^{II}-oxide perovskite derivatives feature $S = 1/2$ spins in a square lattice. Famously, members of this family display a high-temperature superconducting transition induced by electron[17] or hole[18] doping. A similar electronic structure to that of electron-doped oxide cuprates may be accessible in the halide perovskites by incorporating both Cu^+ and Cu^{2+} as B-site cations, which, to our knowledge, has not yet been accomplished. Here, we achieve this mixed-valence Cu state in an unusual layered perovskite containing three distinct metal cations disordered over the octahedral B sites with the formula: $A_4^I[Cu^{II}(Cu^IIn^{III})_{0.5}Cl_8]$ (1; A = organic cation). Perovskite 1 may be derived from the layered Cu^I–In^{III} double perovskite by replacing half of the octahedral metal sites with Cu^{2+}, or equivalently from the layered Cu^{II} perovskites by replacing half of the Cu^{2+} sites with an equal mixture of Cu^+ and In^{3+}. Importantly, spectroscopic characterization of 1 demonstrates that incorporation of three heterovalent B-site cations affords unique optical and electronic properties including enhanced optical absorption in the visible region (Fig. 1) and substantially increased electronic conductivity. We uncover the origins of the new optical, transport, and magnetic properties in 1 and propose a packing model that explains why the specific 1 : 2 : 1 $Cu^+ : Cu^{2+} : In^{3+}$ metal ratio is stabilized in the layered perovskite lattice.

2.   Results and discussion

2.1.   Perovskite structure

The 3D $A^IB^{II}X_3$ single perovskite structure consists of a lattice of corner-sharing BX_6 octahedra (B = divalent cation, X = halide anion) where small monovalent A-site cations fill the voids between octahedra. In the double perovskite structure, the B site is split into two different occupants that form an ordered arrangement yielding the general formula $A_2BB'X_6$. The B and B' sites can be vacant or filled by cations with charges of 1+

through 5+,[19–21] provided that the B sites maintain an average charge of 2+. Employing large alkylammonium A-site cations in the synthesis of halide perovskites affords lower-dimensional derivatives where the inorganic perovskite lattice is partitioned by the organic cations, forming structures with two-dimensional (2D), one-dimensional (1D), or zero-dimensional (0D) connectivity.[22] Recently, dimensional reduction of the double perovskite lattice to 2D layered structures with perovskite layers of mono- and bilayer thickness (n = 1 and 2, respectively) has emerged as a handle for diversifying double perovskites.[23,24] In addition to exhibiting unique optoelectronic properties,[24,25] layered double perovskites have greatly expanded the compositional phase space of this materials family due to the greater structural flexibility of the 2D lattice.[25–27] In the 2D structure, coordination spheres have greater freedom to distort and tilt with respect to one another, stabilizing compositions predicted to be unstable in 3D form.[28,29] Here, we exploit the greater structural freedom of the 2D framework to bring three distinct octahedral metal sites into the perovskite lattice.

2.2.   Tracking the black phase in the synthesis of a Cu^I–In^{III} layered double perovskite

The layered double perovskite $(PEA)_4CuInCl_8$ (PEA = phenethylammonium; Fig. 2A),[30] consists of sheets of corner-sharing $[Cu^ICl_6]^{5-}$ and $[In^{III}Cl_6]^{3-}$ octahedra partitioned by bilayers of PEA cations. Crystals of $(PEA)_4CuInCl_8$ grow as colorless plates under an inert N_2 atmosphere (Fig. 1), but we observed the formation of thin, plate-like, black crystals (1_{PEA}) when droplets of the mother liquor in Paratone-N® oil were exposed to air for ca. 15 minutes. We hypothesized that formation of this black phase is related to the oxidation of Cu^+ to Cu^{2+} and therefore attempted to prepare it directly. (A recent study on a layered Cu^I–In^{III} perovskite also speculated that oxidation of Cu^+ led to formation of black material, although this product was not characterized further.)[31] Indeed, quickly cooling a 100 °C solution of CuCl, $CuCl_2$, In_2O_3, and phenethylamine in HCl under N_2 affords black plate-like crystals (see ESI†). Unfortunately, these crystals diffracted poorly, yet slowing the cooling rate or allowing the black crystals to remain in the mother liquor afforded colorless crystals, hindering characterization and suggesting that the black phase was a kinetic product. Given the importance of the organoammonium A-site cation in dictating both the stability and crystallinity of perovskite phases,[22,25,32,33] we sought to stabilize the black phase using different organic cations. In Sections 2.3 and 2.4, we prepare this black phase using two different organic cations. With butylammonium (BA) cations, we obtain a stable, phase-pure perovskite (1_{BA}) enabling accurate compositional characterization. However, we obtained higher-quality single-crystal X-ray diffraction (SCXRD) data using p-chloroanilinium (PCA) as the A-site cation, and thus, we used this analogue (1_{PCA}) to study structural details.

2.3.   Composition of 1

2.3.1.   SCXRD analysis of 1_{BA}. Similar to the PEA system, colorless crystals form from a slowly cooled solution of CuCl, In_2O_3, and butylamine in HCl under an N_2 atmosphere. SCXRD
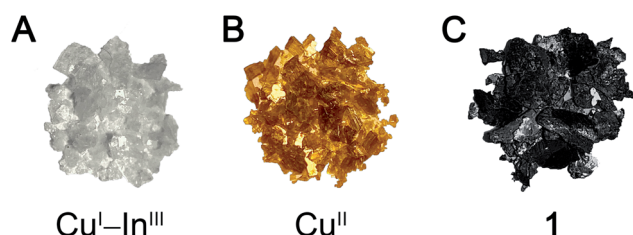

Fig. 1   Photographs of crystals of (A) the colorless double perovskite, $(PEA)_4Cu^IIn^{III}Cl_8$, (B) the yellow single perovskite, $(PCA)_2Cu^{II}Cl_4$, and (C) the black perovskite, $(BA)_4[Cu^{II}(Cu^IIn^{III})_{0.5}Cl_8]$ (1_{BA}), featuring a 1 : 1 blend of the inorganic lattices in A and B. The black color arises from $Cu^{+/2+}$ mixed valency. PEA = phenethylammonium, PCA = p-chloroanilinium, and BA = butylammonium.
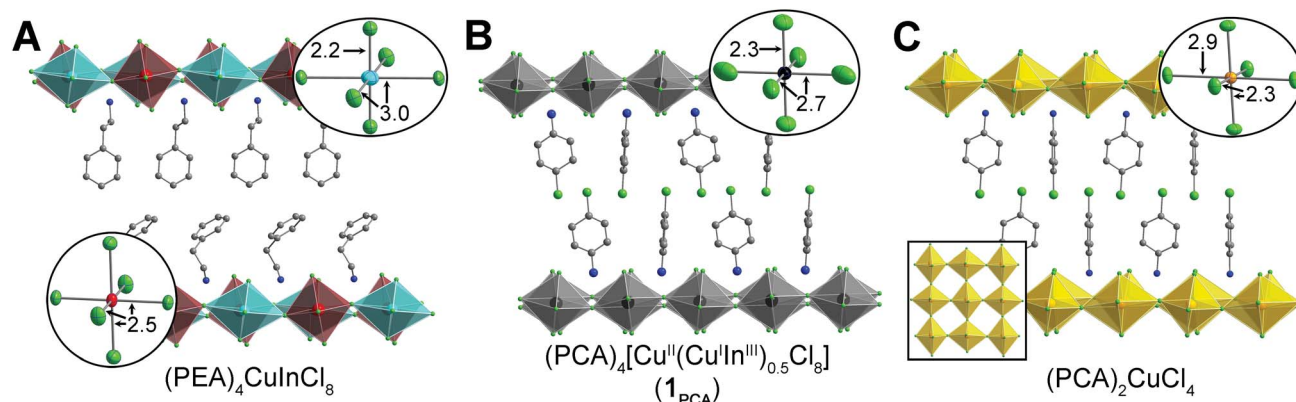
Fig. 2 SCXRD structures of (A) $(PEA)_4CuInCl_8$,[30] (B) $(PCA)_4[Cu^{II}(Cu^IIn^{III})_{0.5}Cl_8]$ (1_{PCA}), and (C) $(PCA)_2CuCl_4$ (ref. 36) at 300 K with insets showing the local coordination environments of the B sites in each structure and the antiferrodistortive arrangement of the elongated axes of the Cu^{2+} octahedra in $(PCA)_2CuCl_4$ (C). Turquoise, red, yellow, green, gray, and blue spheres represent Cu^+, In^{3+}, Cu^{2+}, Cl, C, and N atoms, respectively. Black spheres represent mixed Cu/In sites. H and disordered atoms are omitted for clarity.

analysis of these colorless crystals reveals a dimensionally reduced analog of the hypothetical $A_2^ICu^IIn^{III}Cl_6$ 3D double perovskite, $(BA)_4[Cu_{0.5}InCl_7][Cu_{0.5}Cl][(BA)Cl]$. This structure consists of infinite 1D ribbons of corner-sharing $[CuCl_6]^{5-}$ and $[InCl_6]^{3-}$ octahedra separated by $CuCl_2^-$ monomers (see Fig. S1 and ESI;† note that this phase differs from the layered $(BA)_2(Cu^IIn^{III})_{0.5}Cl_4$ perovskite obtained through a solid-state synthesis).[31] However, when this same precursor solution is exposed to air, we observe the formation of black rectangular plate-like crystals (1_{BA}, Fig. S2†). An air-free solution-state approach where Cu^+, Cu^{2+}, and In^{3+} precursors are combined in HCl with butylamine also affords black crystals (see ESI†). Importantly, unlike 1_{PEA}, crystals of 1_{BA} can be formed by slowly cooling the mother liquor and do not convert to a colorless phase over time.

Single-crystal structure determination of 1_{BA} was complicated by weak diffraction, disorder, and a low-temperature phase transition (see ESI†). Nevertheless, our data reveal that 1_{BA} has an $n = 1$ layered perovskite structure consisting of 2D sheets of corner sharing metal-halide octahedra partitioned by bilayers of BA cations (Fig. S3†). Interestingly, the structure is best modeled when the B sites are treated as a disordered mixture of Cu and In cations. Although too much emphasis should not be placed on structural parameters extracted from this solution due to the relatively low data quality, we were nevertheless intrigued by the ca. 78 : 22 Cu : In site-occupancy ratio found for the B sites (Table S1†). This ratio is very different than the 50 : 50 ratio expected for a disordered $n = 1$ perovskite with only Cu^+ and In^{3+} at the B sites. Because 1_{BA} forms only in the presence of Cu^{2+}, we posited that Cu^{2+} cations could replace equal amounts of In^{3+} and Cu^+ in the perovskite lattice, thus altering the Cu : In occupancy ratio of the B site (see Section 2.4 for an in-depth structural analysis of 1 performed on a higher-quality SCXRD data set).

2.3.2. EPR and XAS analysis of 1_{BA}. The 77 K electron paramagnetic resonance (EPR) spectrum of 1_{BA} (Fig. 3A) confirms incorporation of Cu^{2+} into this material, showing a single feature with an axial spectral shape, where $g_\parallel = 2.06$ and

$g_\perp = 2.16$. These values are nearly identical to those extracted from the spectrum of $(BA)_2Cu^{II}Cl_4$, indicating the presence of exchange-coupled Cu^{2+} centers[34,35] in 1_{BA}. Note that the parallel and perpendicular directions are defined with respect to the unique axis of the perovskite structure ($g_\perp$ refers to the plane of the 2D perovskite sheets while $g_\parallel$ refers to the direction perpendicular to the sheets) rather than that of the Jahn–Teller distorted $[Cu^{II}Cl_6]^{4-}$ unit. By integrating the EPR spectrum of 1_{BA} and using the integrated spectrum of $(PCA)_2Cu^{II}Cl_4$ as a standard, the weight% of Cu^{2+} in 1_{BA} was calculated to be 7.79% (see Fig. S4 and the ESI†). This value agrees within experimental error with the expected value of 8.67% for the formula $(BA)_4[Cu^{II}(Cu^IIn^{III})_{0.5}Cl_8]$ which we calculate below using inductively coupled plasma mass spectrometry (ICP-MS) data (Section 2.3.3).

X-ray absorption spectroscopy (XAS) was also used to confirm the presence of both Cu^+ and Cu^{2+} in 1_{BA} and to estimate the $Cu^+ : Cu^{2+}$ ratio. Measurements were collected at the Cu K-edge on finely ground powders of 1_{BA}, $(EDBE)Cu^{II}Cl_4$ (EDBE = 2,2′-(ethylenedioxy)bis(ethylammonium)), and $(PEA)_4Cu^IIn^{III}Cl_8$, with the latter two materials serving as Cu^{2+} and Cu^+ standards, respectively (see ESI†). Here, we report data obtained using the total electron yield (TEY) method; similar results were obtained using the fluorescence method (Fig. S5 and Table S3†). We found that samples of 1_{BA}, which were phase-pure by PXRD, could be prepared using a range of precursor stoichiometries (see ESI†), and we tested these for compositional variability using XAS. Phase-pure samples of 1_{BA} prepared using high ($Cu^{2+} : Cu^+ : In^{3+}$ ratio of ca. 1 : 2 : 3) and low ($Cu^{2+} : Cu^+ : In^{3+}$ ratio of ca. 1 : 10 : 10) concentrations of Cu^{2+} yield very similar XAS spectra (Fig. 3B). Both feature absorption onsets intermediate between those of the Cu^+ and Cu^{2+} standards, indicating the presence of both oxidation states in 1_{BA}. We fit these spectra using a linear combination of the Cu^+ and Cu^{2+} standard spectra (see ESI†), obtaining estimated $Cu^+ : Cu^{2+}$ ratios of 22 : 78 and 27 : 73 for high and low Cu^{2+} solution concentrations, respectively (Fig. 3C and S6†). These ratios are only estimates as they assume that the Cu^+ and Cu^{2+} environments in
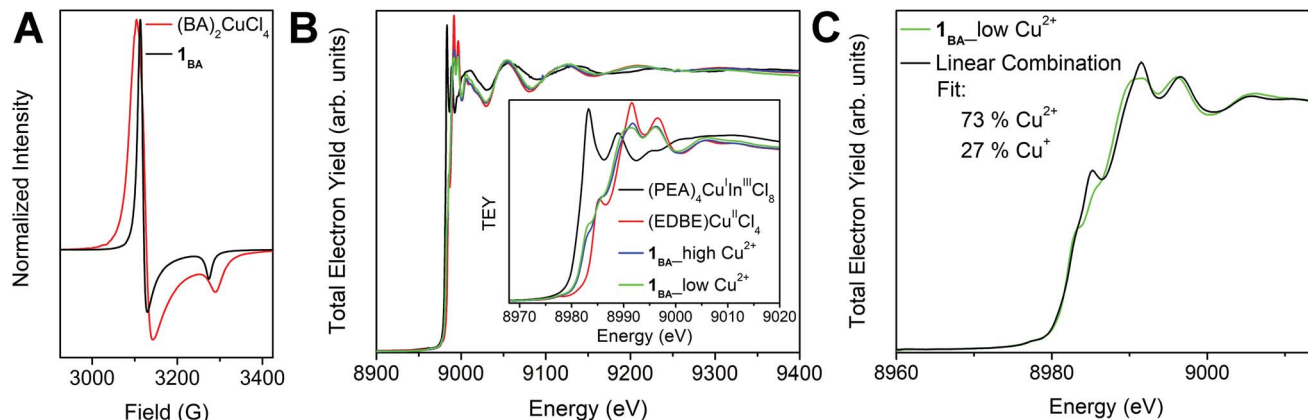
Fig. 3 (A) EPR spectra of 1_{BA} (black) and $(BA)_2CuCl_4$ (red). (B) XAS spectra of $(PEA)_4CuInCl_8$ (black), $(EDBE)CuCl_4$ (red), and 1_{BA} prepared using high (blue) and low (green) solution concentrations of Cu^{2+} (EDBE = 2,2′-(ethylenedioxy)bis(ethylammonium)). (C) A linear combination of the $(PEA)_4CuInCl_8$ and $(EDBE)CuCl_4$ XAS spectra (black) provides an approximation to the XAS spectrum of 1_{BA} prepared using a low solution concentration of Cu^{2+} (green), giving a rough estimate of the $Cu^{2+} : Cu^+$ ratio (73 : 27) for this sample (see Section 2.3.3 for a more accurate value).

1_{BA} are identical to those in the Cu^+ and Cu^{2+} standards. Notably, these results indicate relatively little flexibility in the $Cu^+ : Cu^{2+}$ ratio of 1_{BA} despite the widely ranging precursor ratios employed in the different syntheses.

2.3.3. Elemental analysis of 1_{BA}. To accurately measure the Cu : In ratio of 1_{BA}, we used inductively coupled plasma mass spectrometry (ICP-MS). We measured the same samples made with high and low Cu^{2+} concentrations used for XAS, finding Cu : In weight % ratios of 1.73 and 1.59, respectively (Table S4†). Assuming that all Cu^+ B-site cations are charge compensated by In^{3+} B-site cations, these ratios yield extremely similar formulas of $(BA)_4[(Cu^{II})_{1.04}(Cu^IIn^{III})_{0.48}Cl_8]$ and $(BA)_4[(Cu^{II})_{0.97}(Cu^IIn^{III})_{0.515}Cl_8]$, respectively (see ESI†). Formulas extracted from our SCXRD and XAS data (see ESI†) are consistent with these results, though the ICP-MS formulas are the most reliable given the greater accuracy of this method for such analyses.

Importantly, both our XAS and ICP-MS data indicate little variability in the B-site composition of 1_{BA} and we propose the approximate formula of $(BA)_4[Cu^{II}(Cu^IIn^{III})_{0.5}Cl_8]$. In addition, EPR spin quantification (Section 2.3.2) and magnetic susceptibility measurements (Section 2.6.3) provide two independent estimates of the amount of Cu^{2+} in 1_{BA}, both of which agree with this empirical formula. This validates our assumption that charge balance of the perovskite lattice is maintained by incorporating equal amounts of In^{3+} and Cu^+ at the B sites. Furthermore, C, H, and N analyses of 1_{BA} agree well with our proposed formula (see ESI†). Therefore, our analysis indicates that, in terms of composition, 1_{BA} is a 50 : 50 mixture of a Cu^{II} single perovskite and a $Cu^I–In^{III}$ double perovskite.

2.4. Structure of 1

2.4.1. SCXRD analysis of 1_{PCA}. Crystallizing **1** with *p*-chloroanilinium (PCA) rather than BA also affords black plate-like crystals (1_{PCA}), which provided much higher-quality SCXRD data than 1_{BA} (Table S2†). The structure of 1_{PCA} is

analogous to that of 1_{BA}, with $n = 1$ perovskite sheets partitioned by bilayers of PCA cations (Fig. 2B). At 300 K, the asymmetric unit contains only one unique B site, which is best modeled as a disordered mixture of Cu and In cations (17% In, 83% Cu) and shows two short axial B–Cl_{ax} bonds (2.2790(1) Å) and four long B–Cl_{eq} equatorial bonds (2.6600(1) Å, 2.6593(1) Å; Fig. 2B, inset). Upon cooling to 100 K, the material undergoes a phase transition from $P2_1/c$ to $Pccn$, but the essential features of the structure remain unchanged: we find one unique B site (best modeled as 22% In, 78% Cu) with a similar coordination geometry (Fig. S7†).

Further characterization of 1_{PCA} using the techniques employed above for 1_{BA} was hindered by its instability in solution (similar to the case of 1_{PEA}, see ESI†). Nevertheless, our structural data for 1_{PCA} are fully consistent with the presence of both Cu and In cations at the B sites, and the Cu : In ratio of 78 : 22 (100 K structure) is in good agreement with our ICP-MS data for 1_{BA}.

We can glean further insights into the black phase from the SCXRD structure of 1_{PCA}. At both 300 and 100 K, the structure of 1_{PCA} has only one unique B site, indicating that the Cu^{2+} cations disrupt the checkerboard-like ordering of Cu^+ and In^{3+} cations found in the double-perovskite endmember. As seen in the SCXRD structures of the Cu^{II} and $Cu^I–In^{III}$ endmember perovskites, these three B-site cations exhibit very different coordination environments. The Cu^+ cations of $(PEA)_4CuInCl_8$ adopt a linear $[2 + 4]$ coordination, with two short axial bonds and four long equatorial bonds (Fig. 2A).[30] Meanwhile, the elongated axis of the Jahn–Teller distorted Cu^{2+} cations of $(PCA)_2CuCl_4$ (ref. 36) (and other Cu^{II} perovskites)[37] lies in the plane of the 2D perovskite sheets with the long axes of adjacent $[CuCl_6]^{4-}$ units positioned orthogonally to one another (an anti-ferrodistortive arrangement; Fig. 2C). In contrast, the In^{3+} cations of $(PEA)_4CuInCl_8$ (ref. 30) (and other known $n = 1$ perovskite structures)[25,26] display relatively little deviation from octahedral coordination, with similar axial and equatorial bond lengths (Fig. 2A). Disordering of Cu^+, Cu^{2+}, and In^{3+} is expected

to yield a B-site coordination environment that is an average of the three very different coordination spheres of these cations, with two axial B–Cl$_{ax}$ bonds that are substantially shorter than the four equatorial B–Cl$_{eq}$ bonds. This is, in fact, what we observe in both the 300 and 100 K SCXRD structures of 1_{PCA}. Also consistent with this picture, we find that the thermal ellipsoids of the equatorial Cl atoms are elongated along the directions of B–Cl–B connectivity (Fig. 2B, inset and Fig. S7†) due to the presence of both very long (Cu^{II}–Cl$_{eq}$ = 2.9041(7) Å for (PCA)$_2$CuCl$_4$ at 300 K, Cu^{I}–Cl$_{eq}$ = 3.0340(2) Å for (PEA)$_4$CuInCl$_8$ at 300 K) and very short (Cu^{II}–Cl$_{eq}$ = 2.3067(6) Å for (PCA)$_2$CuCl$_4$ at 300 K) B–Cl$_{eq}$ bond lengths. The thermal ellipsoids of the axial Cl atoms are less elongated, as expected based on the smaller variation in B–Cl$_{ax}$ bond lengths between the Cu$^+$, Cu^{2+}, and In^{3+} coordination spheres of the Cu^{I}–In^{III} and Cu^{II} endmember perovskites (Cu^{I}–Cl$_{ax}$ = 2.1779(1) Å, Cu^{II}–Cl$_{ax}$ = 2.2674(7) Å, In^{III}–Cl$_{ax}$ = 2.5483(1) Å at 300 K).

Although we performed this in-depth structural analysis for 1_{PCA} rather than for 1_{BA} due to the higher-quality SCXRD data obtained for the former, it is important to note that the structural parameters obtained from the SCXRD structure of 1_{BA} are extremely similar (see ESI†), and thus, the above analysis can be extended to the case of 1_{BA}.

2.5. Impact of tiling three coordination spheres on the composition of 1

It is interesting to consider how the very differently shaped Cu$^+$, Cu^{2+}, and In^{3+} coordination spheres (Fig. 4A) can be arranged into an $n = 1$ perovskite lattice. The metal-halide octahedra pack efficiently in (PEA)$_4$CuInCl$_8$ and (PCA)$_2$CuCl$_4$, with the large [Cu^{I}Cl$_6$]$^{5-}$ and small [In^{III}Cl$_6$]$^{3-}$ units adopting an alternating checkerboard pattern in the former and the elongated [Cu^{II}Cl$_6$]$^{4-}$ units forming an antiferrodistortive arrangement in the latter. However, mixing these three units in a single 2D lattice disturbs both of these well-defined arrangements. The elongated [Cu^{II}Cl$_6$]$^{4-}$ units do not fit the Cu^{I}–In^{III} perovskite lattice, introducing large packing mismatch (Fig. 4B). Likewise,

[Cu^{I}Cl$_6$]$^{5-}$ and [In^{III}Cl$_6$]$^{3-}$ units disturb the arrangement of Jahn–Teller distorted [Cu^{II}Cl$_6$]$^{4-}$ octahedra (Fig. 4C). However, a new efficiently packed arrangement can be generated from the cell outlined in Fig. 4D that contains one [In^{III}Cl$_6$]$^{3-}$, one [Cu^{I}Cl$_6$]$^{5-}$, and two [Cu^{II}Cl$_6$]$^{4-}$ units. This cell can be tessellated in two dimensions to generate an $n = 1$ perovskite lattice with no significant packing mismatch. Notably, the resulting lattice has a 1 : 2 : 1 ratio of Cu$^+$: Cu^{2+} : In^{3+} cations, matching the results of our ICP-MS data for 1_{BA} (Section 2.3.3). Thus, we propose that the problem of packing the differently shaped Cu$^+$, Cu^{2+}, and In^{3+} coordination spheres into an $n = 1$ perovskite lattice explains the robust composition adopted by 1_{BA}: a composition in which 50% of the B sites of the Cu^{I}–In^{III} perovskite are replaced by Cu^{2+} cations represents a sweet spot that enables the most efficient packing arrangement of the different coordination spheres. Deviations from this composition will introduce packing mismatch (see ESI and Fig. S8†), which may explain the lack of compositional flexibility observed for 1_{BA}.

Slight variations on the tessellation pattern illustrated in Fig. 4D are also possible, generating 2D lattices with different packing arrangements (Fig. S9†). Some of these packing arrangements are expected to be similarly favorable (Fig. S9B and C†) which may explain the B-site disordering of 1. It is also important to point out that 1, (PCA)$_2$CuCl$_4$, and (PEA)$_4$CuInCl$_8$ all exhibit similar degrees of octahedral tilting, making it unlikely that large packing mismatches are present in 1 as they would likely need to be compensated by severe octahedral tilting.

2.6. Emergent properties in 1

Our characterization of 1_{BA} and 1_{PCA} has shown that the composition and structure of these materials are well-described as an average of the Cu^{II} and Cu^{I}–In^{III} endmember perovskites. However, 1 displays new optical, electronic, and magnetic properties not seen in the endmembers.

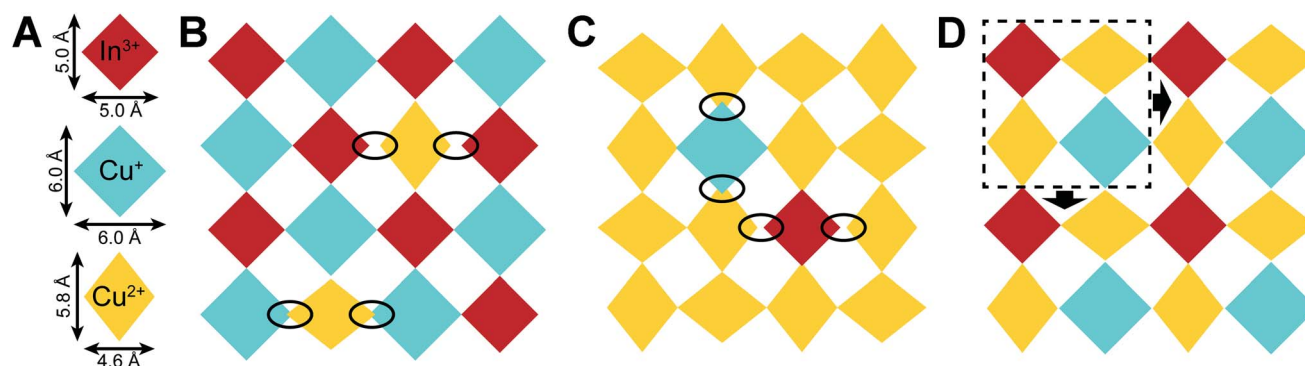**2.6.1. Optical absorption.** The optical absorption of 1 presents a dramatic contrast to that of (BA)$_2$CuCl$_4$ and

Fig. 4 Schematic top-down view of $n = 1$ perovskite sheets where [In^{III}Cl$_6$]$^{3-}$, [Cu^{I}Cl$_6$]$^{5-}$, and [Cu^{II}Cl$_6$]$^{4-}$ units are represented by red, blue, and yellow diamonds, respectively, with dimensions proportional to the coordination spheres found in the 300 K SCXRD structures of (PEA)$_4$CuInCl$_8$ and (PCA)$_2$CuCl$_4$ (A). (B) Packing arrangements for Cu^{2+} doped into the Cu^{I}–In^{III} perovskite lattice and (C) Cu$^+$ and In^{3+} doped into the Cu^{II} perovskite lattice. Large packing mismatches are circled. (D) Proposed packing arrangement for 1: One [In^{III}Cl$_6$]$^{3-}$, one [Cu^{I}Cl$_6$]$^{5-}$, and two [Cu^{II}Cl$_6$]$^{4-}$ units can be arranged into a cell and tessellated to yield a 2D lattice without large packing mismatch. See Fig. S9† for alternative tessellations of the same cell, which may explain the B-site disordering of 1.

$(PEA)_4CuInCl_8$ and cannot be described as a simple average. Whereas $(BA)_2CuCl_4$ and $(PEA)_4CuInCl_8$ are translucent yellow and colorless, respectively, 1_{BA} and 1_{PCA} are black (Fig. 1). We used diffuse reflectance spectroscopy and thin-film transmission measurements to understand the optical behavior of these black perovskites (see ESI† for experimental details). Consistent with its black color, the diffuse reflectance spectrum of 1_{BA} exhibits strong absorption across the entire visible region, displaying features centered at 2.0 eV (with a shoulder at 1.5 eV) and 3.3 eV (Fig. 5A). Similar to prior reports on 2D Cu^{II} perovskites, the diffuse reflectance spectrum of $(BA)_2CuCl_4$ exhibits features centered at *ca.* 1.5 eV and 3.3 eV (Fig. 5A) attributed to d–d and ligand-to-metal charge transfer (LMCT) transitions, respectively.[38,39] Overlaying the spectra of 1_{BA} and $(BA)_2CuCl_4$ points out their obvious similarities: the peak at 1.5 eV in $(BA)_2CuCl_4$ coincides with the low-energy shoulder of the peak at 2 eV in 1_{BA}, and both materials display matching features at *ca.* 3.3 eV. The only significant difference is the broad feature in 1_{BA} centered at 2 eV (Fig. 5A). Unlike the weak Laporte forbidden d–d transitions of Cu^{II} perovskites, this feature is also clearly apparent in the thin-film transmission spectrum of 1_{BA} (though it is shifted to somewhat higher energy, Fig. S10†), indicating that it arises due to a strong absorption event.

Materials containing the same element in multiple valence states that are in electronic contact often exhibit intense colors because electron transfer between the different ions results in strong optical absorption in the visible region.[40] Thus, we propose that the feature at 2 eV in 1_{BA} arises due to the presence of both Cu^+ and Cu^{2+} cations in 1_{BA} and assign it as a $Cu^+ \rightarrow Cu^{2+}$ intervalence charge transfer (IVCT) transition.[41] Intriguingly, this IVCT transition endows crystals of 1_{BA} with clear dichroic effects. Under linearly polarized light, thick plate-like single crystals of 1_{BA} appear black when viewed face-on but translucent red-orange when viewed in the proper side-on orientation (Fig. 5A, inset). This indicates that the 2 eV transition can only be excited by light polarized in the plane of the perovskite sheet and thus corresponds to an IVCT transition between Cu ions in the same layer.

According to the Robin and Day classification,[40] **1** is best described as a class II mixed-valence material. The spectral features of the component ions (most notably the d–d and LMCT transitions of the $[CuCl_6]^{4-}$ unit) are preserved in the mixed-valence material, while a new IVCT absorption appears in the visible region at a location close to that observed for similar class II mixed-valent $Cu^{+/2+}$ materials.[41–43] Assignment of **1** as a class II species is consistent with our structural characterization, which suggests that Cu^+ and Cu^{2+} cations retain distinct coordination environments (excluding assignment as a class III material) but are both six-fold coordinated making structural rearrangement of the coordination spheres relatively easy (unlike in a class I material). Thus, **1** joins the small number of class II mixed-valence halide perovskites, including lattices with $Au^{+/3+}$ and $Sb^{3+/5+}$.[15,40,44]

2.6.2. Electronic conductivity. Mixed valency is well known to significantly alter the electronic properties of a material relative to single-valent counterparts.[40] We therefore used potentiostatic electrochemical impedance spectroscopy (PEIS) to measure the electronic conductivity of large single crystals of 1_{BA}, $(PEA)_4CuInCl_8$, and $(PA)_2CuCl_4$ (PA = propylammonium) painted with carbon contacts as nonreactive, ion-blocking electrodes (Fig. S11†). Single crystals of $(PEA)_4CuInCl_8$ and $(PA)_2CuCl_4$ are highly insulating, and even under 1 V bias, these materials exhibited immeasurably low electronic conductivity (Fig. S12†). This is consistent with a prior report of extremely low (*ca.* 10^{-12} S cm^{-1}) ionic conductivity for crystals of $(NH_3(CH_2)_2NH_3)CuCl_4$ with silver contacts.[45] In contrast, for three different single crystals of 1_{BA}, we measure an average electronic conductivity of *ca.* 8×10^{-9} S cm^{-1} at ambient temperature (see ESI†). This conductivity increases with gentle heating (Fig. 5B, Table S6†) as expected for a semiconductor. Arrhenius plots for these three crystals yield an average activation energy (E_a) of *ca.* 600 meV (Fig. 5C, see ESI†), similar to the value obtained for a related mixed valence chlorocuprate material.[43] Notably, this E_a is close to one-quarter of the energy required for optical excitation (E_{op}) of the $Cu^+ \rightarrow Cu^{2+}$ transition extracted from thin-film measurements (2.28 eV, $E_a/E_{op} = 0.26$, see ESI† for peak analysis and further details).
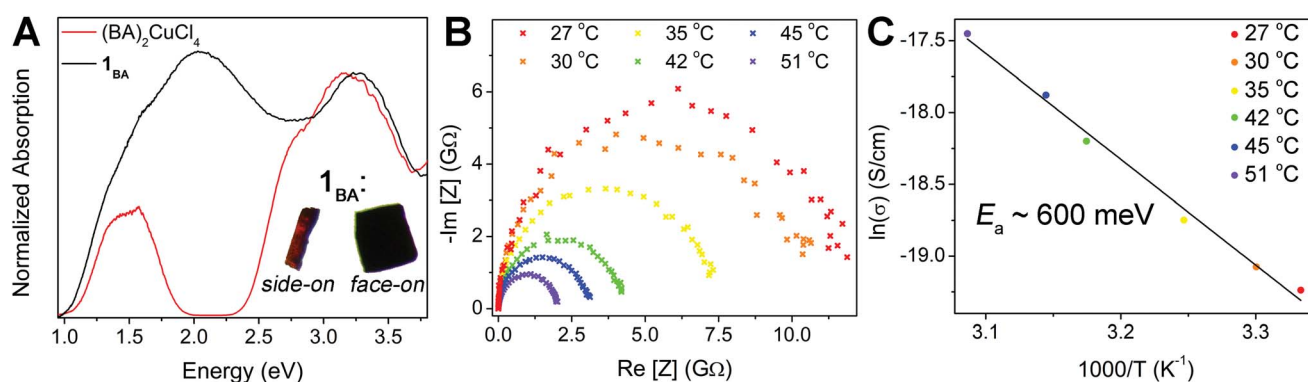

Fig. 5 (A) Diffuse reflectance spectra of 1_{BA} (black) and $(BA)_2CuCl_4$ (red) with insets showing the dichroism of a plate-like crystal of 1_{BA} in side-on and face-on orientations under linearly polarized light. (B) Nyquist plots for a single crystal of 1_{BA} measured at a range of temperatures demonstrating the increase in conductivity with temperature (Z = electrochemical impedance). (C) Arrhenius relationship for the data plotted in B showing an activation energy (E_a) for electronic conductivity (σ) of *ca.* 600 meV.

Previously, Hush developed a theory relating the energy required for thermal electron transfer (corresponding to E_a) to the energy of a vertical Frank–Condon transition (corresponding to E_{op}) for a given IVCT transition.[41] For a symmetric one-electron transfer where the initial and final states have the same energy, E_a/E_{op} is exactly 1/4. Redox asymmetry is expected to yield a larger ratio,[41,46] and is likely at play in $\mathbf{1_{BA}}$. Overall, our data are in good agreement with the work of Hush, providing strong evidence that the enhanced conductivity of $\mathbf{1_{BA}}$ arises due to charge hopping between Cu^+ and Cu^{2+} centers within the same perovskite sheet.

2.6.3. Magnetism. Square 2D lattices of magnetic ions with $S = 1/2$ have long been studied due to their potential to host exotic physics, and as a result, the magnetic properties of Cu^{II} halide perovskites have been heavily investigated over the years.[47,48] Similar to other 2D Cu^{II} perovskites, $(BA)_2CuCl_4$ displays ferromagnetic (FM) ordering (consistent with Goodenough–Kanamori rules)[49–51] below an ordering temperature $T_C = 7.3$ K as well as severe anisotropy between the plane of the inorganic sheets and the axis perpendicular to the sheets, as is expected for these layered materials.[47,48,52] This FM ordering is driven by the dominance of in-plane exchange interactions (over antiferromagnetic exchange interactions between adjacent perovskite layers) and arises from the fact that the unpaired electrons of adjacent Cu^{2+} centers occupy orthogonal orbitals.[48]

Perovskite **1** allows us to test the impact of magnetically diluting this Cu^{2+} square lattice, with nonmagnetic Cu^+ and In^{3+}, on the long-range FM order. Further, $\mathbf{1_{BA}}$ presents an intriguing system for study since the magnetic occupancy of the metal square lattice (approximately 50% Cu^{2+} at the B sites) is close to the site percolation threshold of a 2D simple square lattice with four nearest neighbors (59.2%).[53,54] At and above this value, enough magnetic ions should exist to support long-range magnetic order. While the overall stoichiometry of $\mathbf{1_{BA}}$ is below this threshold, if some areas of the square lattice have a high enough concentration of Cu^{2+} ions, local puddles of long-range order may arise.

Our measurements reveal weak interactions between local Cu^{2+} moments with no long-range order down to $T = 2$ K, as shown by the lack of a peak in plots of the low-temperature zero-field AC susceptibility (Fig. 6A, insets) and low-field DC susceptibility (Fig. 6A). A spin glass ground state, which may also be expected for dilute magnetic ions, is ruled out by the lack of splitting between the zero-field cooled and field cooled susceptibility data at low temperature (Fig. 6A), the lack of a peak in the variable-temperature AC susceptibility (χ' and χ''; Fig. 6A, insets), and the frequency-independence of the AC susceptibility (Fig. S17†). High-temperature DC susceptibility measured in an applied field of $\mu_0H = 5$ T (μ_0 = permeability of free space, H = magnetic field strength) is shown in Fig. 6B. After subtraction of a large temperature-independent diamagnetic contribution (likely from BA cations, $\chi_0 = -0.00108$ emu mol^{-1}) a Curie–Weiss fit of the inverse susceptibility data from $T = 100$–300 K yields a Curie constant $C = 0.362(4)$ K emu mol^{-1} and a Weiss temperature $\Theta = 10.9(2)$ K. Note that these calculations assume a formula weight given by the formula of $\mathbf{1_{BA}}$
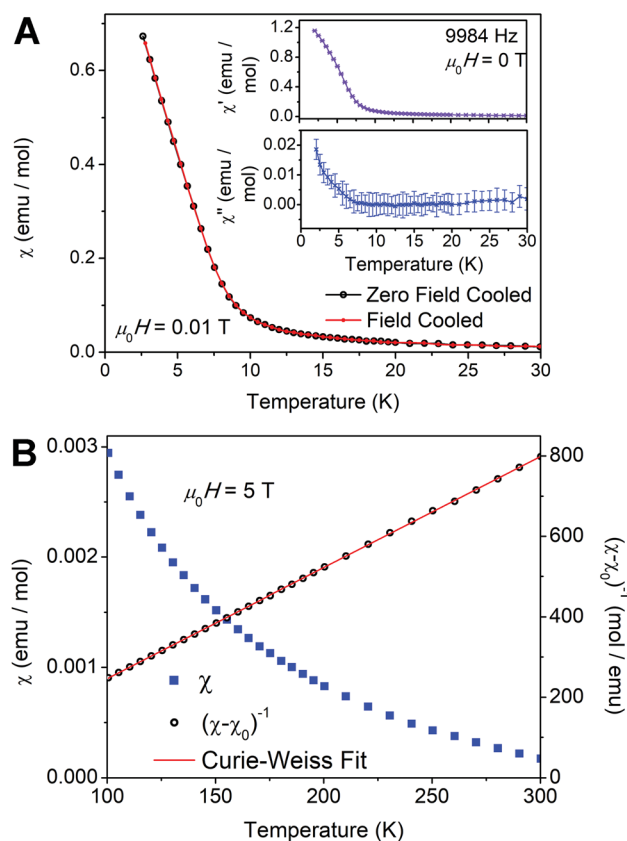

Fig. 6 (A) Zero-field cooled and field cooled DC susceptibility (χ) of $\mathbf{1_{BA}}$ measured in a small applied field ($\mu_0H = 0.01$ T) from $T = 2$–30 K. The top and bottom insets show the real (χ') and imaginary (χ'') parts of the AC susceptibility, respectively, measured in zero applied field. (B) High-temperature DC susceptibility (χ) and inverse susceptibility (($\chi - \chi_0)^{-1}$) of $\mathbf{1_{BA}}$ measured in an applied field $\mu_0H = 5$ T (χ_0 is the diamagnetic contribution to χ).

determined above ($(BA)_4[Cu^{II}(Cu^I In^{III})_{0.5}Cl_8]$). The slightly positive value of Θ may indicate that the weak interactions between moments, or the interactions in somewhat more concentrated puddles, are FM. Our fit results are in line with those reported for $(BA)_2CuCl_4$, which has a higher value of Θ (18.3(3) K), consistent with its long-range FM order at $T_C = 7.3$ K.[47,52] The effective moment (μ_{eff}) of $\mathbf{1_{BA}}$ is 1.702(1) μ_B (μ_B = Bohr magneton), consistent with magnetically isolated Cu^{2+} moments, and the Landé g-factor is 1.965(1), consistent with the g-factors extracted from EPR measurements (Section 2.3.2). The overall paramagnetic behavior and the absence of magnetic long-range order are consistent with our ICP-MS analysis, which yields a Cu^{2+} content below the site percolation threshold. In addition, as noted in Section 2.3.3, our magnetic susceptibility measurements allow us to estimate the amount of Cu^{2+} in $\mathbf{1_{BA}}$ as 0.97 mol Cu^{2+} per formula unit (see ESI†), in agreement with the values obtained from ICP-MS (Section 2.3.3) and EPR data (Section 2.3.2).

These findings present an interesting contrast with a report of an $n = 1$ Zn^{II} fluoride perovskite where 40% of the B sites are replaced with Cu^{2+}. Here, the Cu^{2+} content is well below the site percolation threshold and also lower than that of $\mathbf{1_{BA}}$, yet EPR

data provide evidence for long-range magnetic order at 4.2 K.[55] This suggests that Cu^{2+} cations may form clusters within the Zn^{2+} lattice, leading to the stronger magnetic interactions. The absence of long-range order in $\mathbf{1_{BA}}$ despite the higher Cu^{2+} content suggests that here, Cu^{2+} cluster formation may be disfavored. This further validates our proposed packing scheme discussed in Section 2.5 and the ESI,† which shows that arrangements containing adjacent Cu^{2+} centers generally have larger packing mismatch (Fig. S9D and F†), potentially disfavoring formation of Cu^{2+} clusters.

3. Conclusion

We report the new layered perovskite $(A)_4[Cu^{II}(Cu^{I}In^{III})_{0.5}Cl_8]$ ($\mathbf{1}$, A = BA, PCA, PEA), which contains a 1 : 2 : 1 mixture of Cu^+, Cu^{2+}, and In^{3+} cations at the B sites. The composition and structure of $\mathbf{1}$ are well-described as an average of a Cu^{II} single perovskite and a $Cu^{I}–In^{III}$ double perovskite. Simple packing arguments suggest that this specific composition is enforced by the differently shaped Cu^+, Cu^{2+}, and In^{3+} coordination spheres that must pack efficiently into an $n = 1$ perovskite lattice. Magnetic studies of $\mathbf{1_{BA}}$ demonstrate the loss of long-range ferromagnetic order observed in the Cu^{II} perovskite, corroborating our proposed packing model, which disfavors segregated domains of Cu^{II} in the lattice of $\mathbf{1}$.

The presence of mixed-valent Cu in $\mathbf{1}$ affords new properties not seen in the endmember lattices. In particular, $\mathbf{1}$ is black, displaying strong optical absorption across the visible region, which is highly unusual for an $n = 1$ chloride perovskite. We further measure a large increase in conductivity between $\mathbf{1_{BA}}$ and its Cu^{II} and $Cu^{I}–In^{III}$ endmembers. Thus, alloying two different 2D perovskites affords a new perovskite with properties not seen in either endmember.

The novel optoelectronic properties of $\mathbf{1}$ evidence the significant advantages of incorporating B-site cations with a range of valence states into the perovskite structure and set forth the tantalizing possibility of using this strategy to access exotic physical properties, similar to the discovery of high-temperature superconductivity in analogous electron-doped copper-oxide perovskites. We expect that the simple tiling arguments made here, based on using a mixture of long and short metal-halide bond lengths to construct the 2D footprint of the inorganic sheets, may be extended to other compositions to incorporate multiple metal ions in the perovskite lattice. Thus, increasing the complexity of the inorganic sheets, beyond the simple rock-salt ordering of most double perovskites,[1] promises to enhance the optoelectronic diversity of halide perovskites with emergent properties arising from new electronic transitions.

Author contributions

B. A. C. performed all experimental work and analysis, except as noted below. J. L. synthesized materials for elemental analysis and EPR studies. B. A. C. and J. L. were advised by H. I. K. R. W. S. conducted the magnetic susceptibility measurements and data analysis, advised by Y. S. L. A. J. H. conducted EPR spin

quantification studies. A. G.-P. conducted the XAS measurements and data analysis, advised by M. F. T. The project was conceived by B. A. C. with guidance from H. I. K.; they wrote the manuscript with contributions from all authors.

Conflicts of interest

There are no conflicts to declare.

Acknowledgements

Notes and references

1 N. R. Wolf, B. A. Connor, A. H. Slavney and H. I. Karunadasa, *Angew. Chem., Int. Ed.*, 2021, **60**, 2–17.

2 A. H. Slavney, T. Hu, A. M. Lindenberg and H. I. Karunadasa, *J. Am. Chem. Soc.*, 2016, **138**, 2138–2141.

3 E. T. McClure, M. R. Ball, W. Windl and P. M. Woodward, *Chem. Mater.*, 2016, **28**, 1348–1354.

4 G. Engel, *Naturwissenschaften*, 1933, **21**, 704.

5 A. H. Slavney, L. Leppert, D. Bartesaghi, A. Gold-Parker, M. F. Toney, T. J. Savenije, J. B. Neaton and H. I. Karunadasa, *J. Am. Chem. Soc.*, 2017, **139**, 5015–5018.

6 J. Luo, X. Wang, S. Li, J. Liu, Y. Guo, G. Niu, L. Yao, Y. Fu, L. Gao, Q. Dong, C. Zhao, M. Leng, F. Ma, W. Liang, L. Wang, S. Jin, J. Han, L. Zhang, J. Etheridge, J. Wang, Y. Yan, E. H. Sargent and J. Tang, *Nature*, 2018, **563**, 541–545.

7 K. P. Lindquist, S. A. Mack, A. H. Slavney, L. Leppert, A. Gold-Parker, J. F. Stebbins, A. Salleo, M. F. Toney, J. B. Neaton and H. I. Karunadasa, *Chem. Sci.*, 2019, **10**, 10620–10628.

8 A. H. Slavney, L. Leppert, A. Saldivar Valdes, D. Bartesaghi, T. J. Savenije, J. B. Neaton and H. I. Karunadasa, *Angew. Chem., Int. Ed.*, 2018, **57**, 12765–12770.

9 A. E. Maughan, A. M. Ganose, M. M. Bordelon, E. M. Miller, D. O. Scanlon and J. R. Neilson, *J. Am. Chem. Soc.*, 2016, **138**, 8453–8464.

10 T. T. Tran, J. R. Panella, J. R. Chamorro, J. R. Morey and T. M. McQueen, *Mater. Horiz.*, 2017, **4**, 688–693.

11 K.-z. Du, W. Meng, X. Wang, Y. Yan and D. B. Mitzi, *Angew. Chem., Int. Ed.*, 2017, **56**, 8158–8162.

12 A. Karmakar, M. S. Dodd, S. Agnihotri, E. Ravera and V. K. Michaelis, *Chem. Mater.*, 2018, **30**, 8280–8290.

13 N. Nandha K and A. Nag, *Chem. Commun.*, 2018, **54**, 5205–5208.

14 J. D. Majher, M. B. Gray, T. A. Strom and P. M. Woodward, *Chem. Mater.*, 2019, **31**, 1738–1744.

15 L. Atkinson and P. Day, *J. Chem. Soc. A*, 1969, 2423–2431.

16 M. Retuerto, Z. Yin, T. J. Emge, P. W. Stephens, M.-R. Li, T. Sarkar, M. C. Croft, A. Ignatov, Z. Yuan, S. J. Zhang, C. Jin, R. P. Sena, J. Hadermann, G. Kotliar and M. Greenblatt, *Inorg. Chem.*, 2015, **54**, 1066–1075.

17 N. P. Armitage, P. Fournier and R. L. Greene, *Rev. Mod. Phys.*, 2010, **82**, 2421–2487.

18 C. W. Chu, L. Z. Deng and B. Lv, *Phys. C*, 2015, **514**, 290–313.

19 N. Elliott and L. Pauling, *J. Am. Chem. Soc.*, 1938, **60**, 1846–1851.

20 R. W. G. Wyckoff and E. Posnjak, *J. Am. Chem. Soc.*, 1921, **43**, 2292–2309.

21 K. Prassides, P. Day and A. K. Cheetham, *Inorg. Chem.*, 1985, **24**, 545–552.

22 D. B. Mitzi, *J. Chem. Soc., Dalton Trans.*, 2001, 1–12.

23 L. M. Castro-Castro and A. M. Guloy, *Angew. Chem., Int. Ed.*, 2003, **42**, 2771–2774.

24 B. A. Connor, L. Leppert, M. D. Smith, J. B. Neaton and H. I. Karunadasa, *J. Am. Chem. Soc.*, 2018, **140**, 5235–5240.

25 B. A. Connor, R.-I. Biega, L. Leppert and H. I. Karunadasa, *Chem. Sci.*, 2020, **11**, 7708–7715.

26 L. Mao, S. M. L. Teicher, C. C. Stoumpos, R. M. Kennard, R. A. DeCrescent, G. Wu, J. A. Schuller, M. L. Chabinyc, A. K. Cheetham and R. Seshadri, *J. Am. Chem. Soc.*, 2019, **141**, 19099–19109.

27 L.-Y. Bi, Y.-Q. Hu, M.-Q. Li, T.-L. Hu, H.-L. Zhang, X.-T. Yin, W.-X. Que, M. S. Lassoued and Y.-Z. Zheng, *J. Mater. Chem. A*, 2019, **7**, 19662–19667.

28 G. Volonakis, A. A. Haghighirad, R. L. Milot, W. H. Sio, M. R. Filip, B. Wenger, M. B. Johnston, L. M. Herz, H. J. Snaith and F. Giustino, *J. Phys. Chem. Lett.*, 2017, **8**, 772–778.

29 Z. Xiao, K.-Z. Du, W. Meng, D. B. Mitzi and Y. Yan, *Angew. Chem., Int. Ed.*, 2017, **56**, 12107–12111.

30 M. L. Aubrey, A. Saldivar Valdes, M. R. Filip, B. A. Connor, K. P. Lindquist, J. B. Neaton and H. I. Karunadasa, Directed assembly of layered halide perovskite heterostructures as single crystals, in review.

31 E. T. McClure, A. P. McCormick and P. M. Woodward, *Inorg. Chem.*, 2020, **59**, 6010–6017.

32 L.-Y. Bi, T.-L. Hu, M.-Q. Li, B.-K. Ling, M. S. Lassoued, Y.-Q. Hu, Z. Wu, G. Zhou and Y.-Z. Zheng, *J. Mater. Chem. A*, 2020, **8**, 7288–7296.

33 E. R. Dohner, E. T. Hoke and H. I. Karunadasa, *J. Am. Chem. Soc.*, 2014, **136**, 1718–1721.

34 C.-C. Chao, *J. Magn. Reson.*, 1973, **10**, 1–6.

35 C. P. Landee, K. E. Halvorson and R. D. Willett, *J. Appl. Phys.*, 1987, **61**, 3295–3297.

36 A. K. Vishwakarma, P. S. Ghalsasi, A. Navamoney, Y. Lan and A. K. Powell, *Polyhedron*, 2011, **30**, 1565–1570.

37 R. D. Willett, *J. Chem. Phys.*, 1964, **41**, 2243–2244.

38 R. D. Willett, O. L. Liles Jr and C. Michelson, *Inorg. Chem.*, 1967, **6**, 1885–1889.

39 R. Valiente and F. Rodríguez, *Phys. Rev. B: Condens. Matter Mater. Phys.*, 1999, **60**, 9423–9429.

40 M. B. Robin and P. Day, in *Advances in Inorganic Chemistry and Radiochemistry*, ed. H. J. Emeléus and A. G. Sharpe, Academic Press, 1968, vol. 10, pp. 247–422.

41 N. S. Hush, in *Prog. Inorg. Chem.*, ed. F. A. Cotton, John Wiley & Sons, Inc., 1967, ch. 7, vol. 8, pp. 391–444.

42 M. Mori, *Bull. Chem. Soc. Jpn.*, 1961, **34**, 1249–1253.

43 D. Culpin, P. Day, P. R. Edwards and R. J. P. Williams, *Chem. Commun.*, 1965, 450–451.

44 N. Kojima and H. Kitagawa, *J. Chem. Soc., Dalton Trans.*, 1994, 327–331.

45 C. P. Tigges, J. E. Drumheller and L. O. Snively, *J. Appl. Phys.*, 1983, **54**, 5473–5475.

46 D. M. D'Alessandro and F. R. Keene, *Chem. Soc. Rev.*, 2006, **35**, 424–440.

47 L. J. de Jongh, A. C. Botterman, F. R. de Boer and A. R. Miedema, *J. Appl. Phys.*, 1969, **40**, 1363–1365.

48 L. J. de Jongh and A. R. Miedema, *Adv. Phys.*, 1974, **23**, 1–260.

49 J. B. Goodenough, *Phys. Rev.*, 1955, **100**, 564–573.

50 J. B. Goodenough, *J. Phys. Chem. Solids*, 1958, **6**, 287–297.

51 J. Kanamori, *J. Phys. Chem. Solids*, 1959, **10**, 87–98.

52 C. Aruta, F. Licci, A. Zappettini, F. Bolzoni, F. Rastelli, P. Ferro and T. Besagni, *Appl. Phys. A*, 2005, **81**, 963–968.

53 S. Galam and A. Mauger, *Phys. Rev. E: Stat. Phys., Plasmas, Fluids, Relat. Interdiscip. Top.*, 1996, **53**, 2177–2181.

54 K. Malarz and S. Galam, *Phys. Rev. E: Stat., Nonlinear, Soft Matter Phys.*, 2005, **71**, 016125.

55 D. Reinen and S. Krause, *Inorg. Chem.*, 1981, **20**, 2750–2759.